Materials Horizons

ROYAL SOCIETY OF CHEMISTRY

COMMUNICATION

View Article Online
View Journal | View Issue

Cite this: *Mater. Horiz.*, 2025, **12**, 10839

Received 28th March 2025,
Accepted 29th August 2025

DOI: 10.1039/d5mh00559k

rsc.li/materials-horizons

Smart coacervate catalysis: robotic optimization of Knoevenagel reaction networks

Anna S. Nebalueva,[a] Danila V. Ermolin,[a] Alexandra P. Dergacheva,[a] Alexander S. Novikov,[a] Alexander A. Nikolaev,[a] Bogdan S. Vahrushev,[a] Artemii M. Zenkin,[a] Igor S. Pantyukhin,[a] Alexandr A. Semenov,[a] Aleksei V. Meshkov,[a] Anton A. Muravev,*[a] Daria V. Andreeva *[bc] and Ekaterina V. Skorb *[a]

The emergence of collaborative robotics and additive manufacturing of equipment consumables has had a significant impact on the development of chemical synthesis, biomedicine, the food industry, and agriculture. However, high cost hampers the application of collaborative robots in organic and physical chemistry. Here we suggest a low-cost 3D-printed robotic platform made from gripper and dispenser manipulators coupled with computer vision tools that provide full automation of the Knoevenagel reaction of barbituric acid with aromatic aldehydes, ranging from mixing of reagents to kinetic spectrophotometric monitoring. Screening of conditions of the Knoevenagel reaction between barbituric acid and aromatic aldehydes (reagent ratio, concentration and type of polyelectrolytes and interpolyelectrolyte complexes, as well as type of aromatic aldehyde) powered by the developed open-source Python-based software boosts the discovery of optimal conditions for enhanced reaction kinetics. Our robotic system performs dataset collection and discovers smart polyelectrolyte coacervate catalysis.

New concepts

This study presents a groundbreaking low-cost, 3D-printed robotic platform integrated with computer vision and open-source software to automate the optimization of Knoevenagel reactions. The system combines gripper and dispenser manipulators to enable precise reagent handling, kinetic spectrophotometric monitoring, and high-throughput screening of reaction conditions. Key findings include the discovery that polyelectrolyte coacervates (PDADMAC-PAA) significantly enhance reaction kinetics and a three-fold excess of vanillin boosts the rate constant to 1.46 L mol^{-1} s^{-1}. DFT calculations rationalize the catalytic role of coacervates in stabilizing intermediates. This work bridges robotics, catalysis, and materials science, offering a scalable, frugal solution for automated chemical synthesis.

Introduction

Coacervate complexes, firstly introduced by Oparin to investigate the origin of life,[1] have greatly expanded over recent decades to offer solutions for liquid robotics,[2] wastewater treatment,[3] catalysis,[4] biomimetic adhesives,[5] sensors,[6–8] self-healing membranes,[9,10] and drug delivery,[11] to name just a few. Such versatility emerges from the confined space created by polymer molecules self-organized into a separate phase through electrostatic interactions and explains the enhanced affinity between interacting molecules.[12] Numerous biochemical reactions and some reactions of small organic molecules were shown to accelerate in the bulk coacervate phase, from RNA catalysis[13] to condensation, photodegradation, and reduction.[14–17]

Robotization has had a progressive impact on many fields in chemistry, finally reaching the long-awaited potential to automate organic synthesis—including that of active pharmaceutical ingredients.[18–23] The utilization of robotic and automated systems in chemical experiments offers several advantages, including improvements in precision and reproducibility, contributions to a safer laboratory environment by handling hazardous materials without exposing human researchers to associated risks, reducing resource expenditure, and improving the cost-efficiency of laboratory experiments.[24] A common approach to laboratory automation takes the form of automated chemical reactors, which are used in high-throughput screenings.[25] The high precision of robotic systems and the ease of integrating computational modelling allow for the creation of self-driving laboratories, where predicted experimental outcomes can be verified in real time by a robotic researcher. Another approach to laboratory automation involves the use of multi-purpose articulated robotic manipulators and mobile robotics to conduct experiments. This approach enables the creation of modular, easily reconfigurable laboratories in the pursuit of realizing the self-driving laboratory concept. Following this concept, a collaboration of three different commercially available robots was tasked with completing a full experimental

[a] *ITMO University, Lomonosov str. 9A, St., Petersburg, 191002, Russian Federation. E-mail: muravev@itmo.ru, skorb@itmo.ru*
[b] *Institute for Functional Intelligent Materials, National University of Singapore, 117544, Singapore. E-mail: daria@nus.edu.sg*
[c] *Department of Materials & Science Engineering, National University of Singapore, 117575, Singapore*

cycle in solid-state chemistry research, which included crystal growth, sample preparation, and powder X-ray diffraction data acquisition.[26] Despite the growth of the industrial, service, and laboratory robotization markets, the issue of high initial costs still persists and has been addressed by several researchers worldwide. There is a trade-off between cost and efficiency of robotic laboratory solutions; for instance, the maximum speed of the self-made Gantry Robot had to be limited to maintain its functionality.[27] For systems that mimic the functionality of more expensive and specialized counterparts, researchers have introduced the term "frugal twin" and argue that their modularity and low cost make them a valuable solution for the development of self-driving laboratories, as well as for educational and research purposes.[28] However, there are as yet no works exploring the optimization of coacervate-mediated organic reaction networks, which is a cornerstone of the expansion of the scope of click reactions to different organic substrates.[29]

This study bridges low-cost laboratory automation and soft matter-assisted catalysis and demonstrates for the first time an open-source, 3D-printed robotic system specifically designed and validated for the automation of coacervate-mediated reactions. More specifically, we developed an easy-to-reproduce robotic dispenser and gripper with control software to automate sampling of barbituric acid and aromatic aldehydes and their transfer to a spectrophotometric cuvette for UV/visible spectrophotometric monitoring of the Knoevenagel reaction. Through variation of reagent ratio and the nature of polyelectrolytes that form coacervate complexes, a significant reduction in the time of reaction—up to a few minutes—has been demonstrated under polyelectrolyte crowding conditions and rationalized through quantum-chemical calculations.

Results and discussion

Methodologically, a good candidate for the optimization and automation of organic synthesis is the Knoevenagel reaction between barbituric acid and aromatic aldehydes. Its outcome is sensitive to pH, reagent ratio, and the nature of the substituent on both reagents. In the latter case, electron-donating substituents, such as vanillin **2a**, ethylvanillin **2b**, veratryl **2c**, hydroxyphenyl **2d**, furyl **2e**, and pyrryl **2f** moieties, can be suggested, which afford corresponding Knoevenagel adducts **3a–f** (Fig. 1A). Furthermore, mechanistically similar nucleophilic addition–

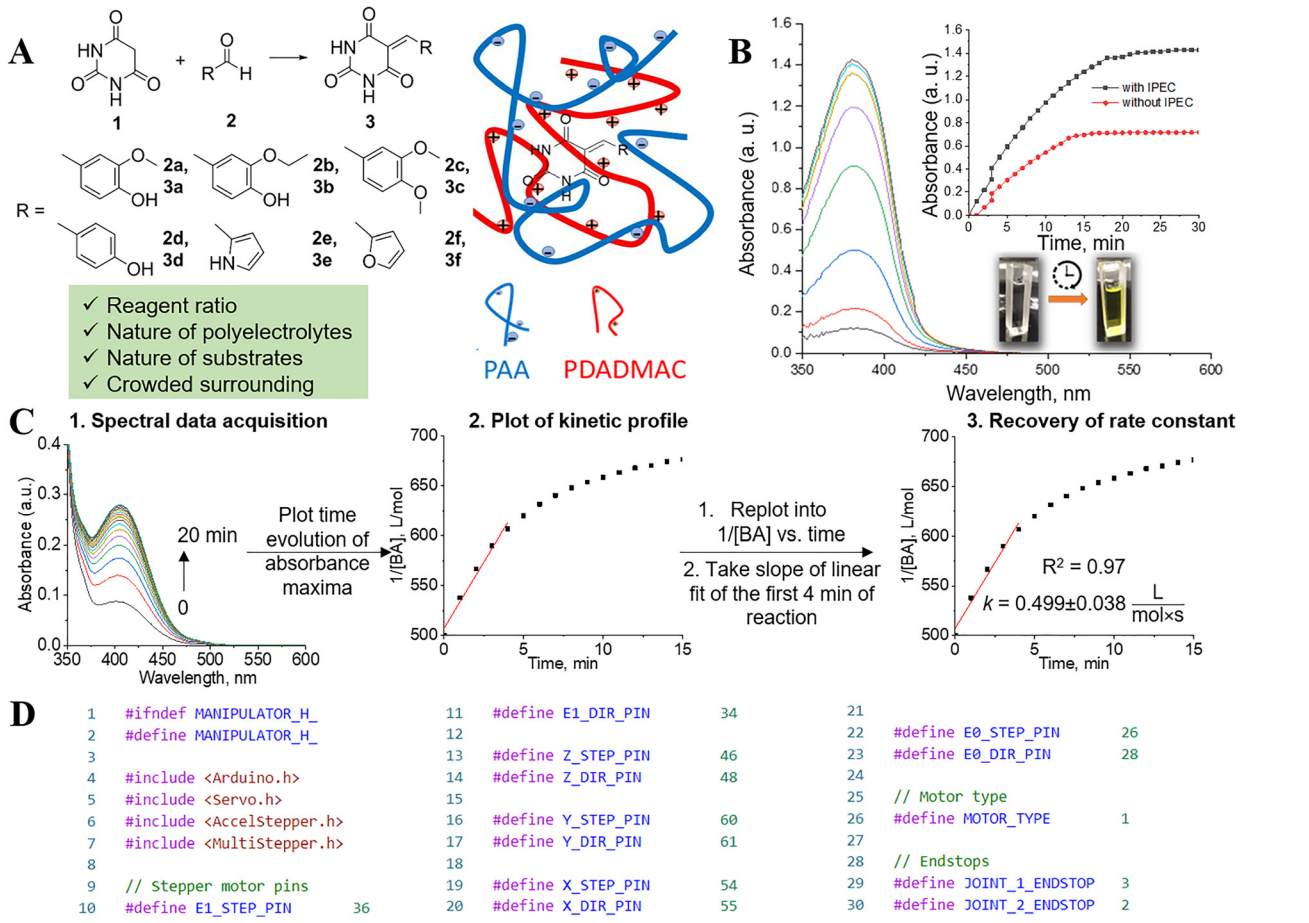

Fig. 1 (A) Scheme of Knoevenagel condensation between barbituric acid (**1**) and aldehydes (**2a–f**) and schematic view of encapsulation of reaction product by interpolyelectrolyte complexes (IPECs). (B) Evolution of UV-visible absorption spectra of formation of compounds **3a–f** with and without IPECs and plot of time evolution of absorbance maxima. (C) Pipeline for determination of reaction rate constant. (D) Fragment of the C++ code for Arduino controller responsible for operation of stepping motors of manipulators.

elimination reactions[14,15] were reported to respond to the crowded coacervate phase as schematically depicted in Fig. 1A for the reaction product **3**, which allows for a wide screening of polyelectrolytes (molecular structure, molecular-mass distribution, and concentration). Finally, the formed Knoevenagel adduct is colored, which allows for the real-time spectrophotometric monitoring of the reaction kinetics and one-factor-at-a-time optimization of the reaction conditions (Fig. 1B). Dynamic spectrophotometric monitoring of the Knoevenagel reaction can be automated by employing the spectra acquisition–concentration-based kinetic profiling-rate constant determination pipeline (Fig. 1C). Regarding industrial relevance, automated screening and optimization of the condensation of barbituric acid and aldehydes is crucial for pharmaceutics, where barbiturates are promising antioxidants,[30] and development of organic piezoelectric materials.[31] Regarding the Knoevenagel reaction, it is a crucial transformation facilitating synthesis of valuable compounds; however, its biomedical application is restricted by its requirement for basic conditions and nonaqueous solvents, and only a few works on protein labeling in living cells[32] *via* this reaction have been reported.

Thus, coacervate catalysis in water is a proof-of-concept study of biorthogonality of Knoevenagel reactions and could boost discovery of new methods of bioconjugation and drug delivery.

Furthermore, robotic synthesis could avoid the variance of collected experimental data due to operator interference and potentially improve repeatability and reproducibility of sample handling in chemical laboratories, as well as provide high-speed automated data acquisition. Open-source software along with additive manufacturing technologies (3D-printing) provide a fascinating potential for the widespread employment of robotic platforms in organic process development. A fragment of C++ code demonstrates the realization of the interface of an Arduino microcontroller that submits commands to stepping motors for initialization and positioning of robotic manipulators (Fig. 1D; a full description of the manipulators' firmware can be found in the SI). We suggested the following design of a robotic platform for the preparation of Knoevenagel reaction mixtures (Fig. 2A; full data of its assembly are provided in Tables S1–S15 and Fig. S1–S83). One manipulator (dispenser, Fig. 2B) is initiated by the drive pulled through a clock switch. The dispenser takes a new tip from stand G, draws an aliquot from the centrifuge tube in rack E (intended for open tubes with individual solutions), transfers it to the tube in rack F (intended for the storage of mixed solutions of reagents), and

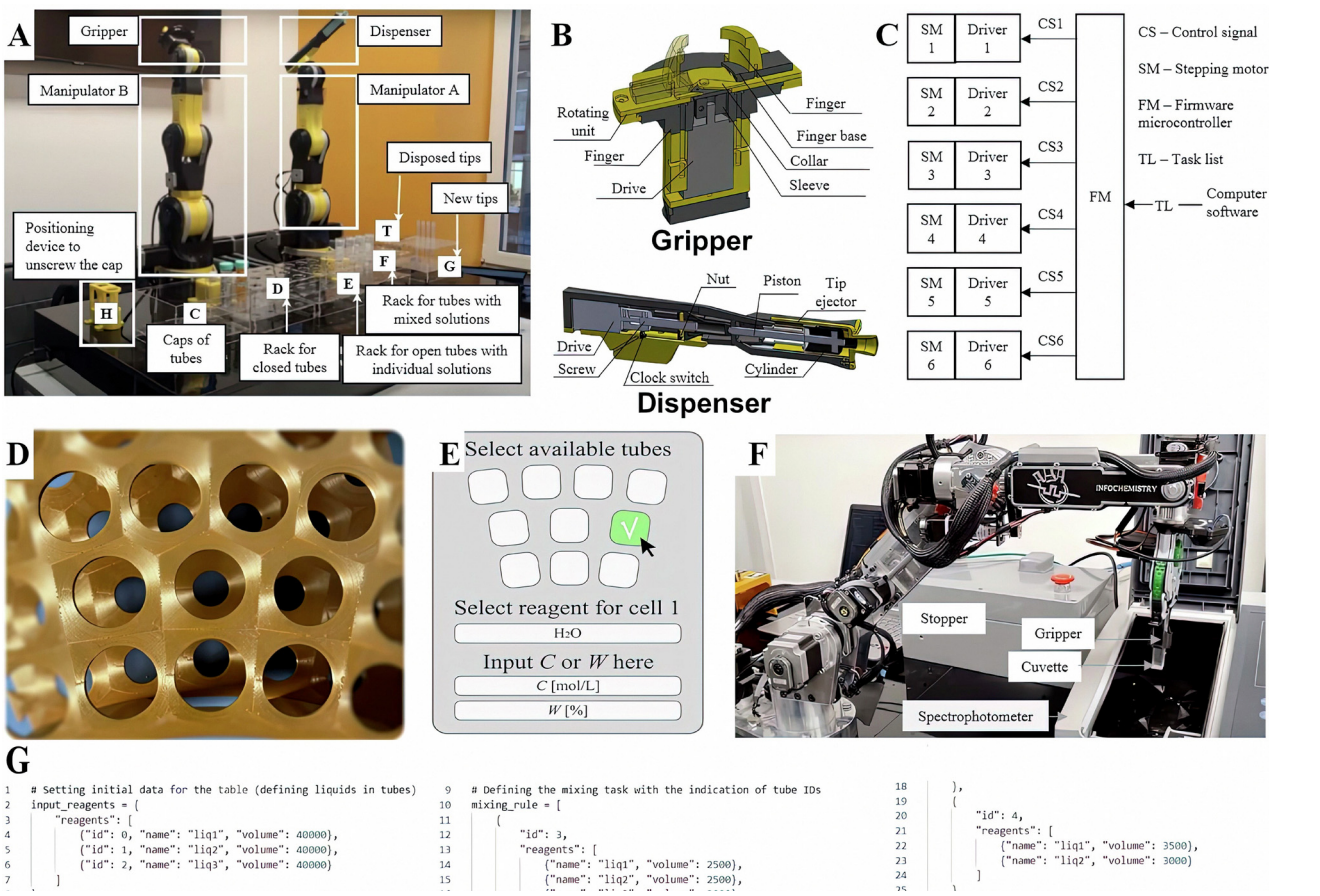

Fig. 2 (A) Robotized stand for sample preparation. (B) Detailed view of gripper and dispenser manipulators. (C) System architecture. (D) 3D-printed test tube rack. (E) Graphical user interface for setting the reagent parameters. (F) Transfer of plastic cuvette with reaction mixture to the spectrophotometer using robotized gripper. (G) Fragment of *json file for the operation of robotized dispenser responsible for the identification of test tube and sampling volume for reagent mixing task.

Table 1 Effect of conditions of the reaction of barbituric acid **1** with different aldehydes **2a–f** on the kinetic rate constant (L mol^{-1} s^{-1})

Entry	Aldehyde	Aldehyde-to-1 molar ratio	Polyelectrolyte	C_{PE} [mg mL^{-1}]	MW_{PE} [kDa]	Rate constant [10^{-2} L mol^{-1} s^{-1}]
1	**2a**	1 : 1	—	—	—	50.0 ± 4.9
2	**2a**	1 : 2	—	—	—	87.8 ± 5.3
3	**2a**	1 : 3	—	—	—	83.9 ± 3.5
4	**2a**	2 : 1	—	—	—	63.7 ± 1.9
5	**2a**	3 : 1	—	—	—	146.2 ± 1.9
6	**2a**	1 : 1	PDADMAC	2.0	100	30.7 ± 0.5
7	**2a**	1 : 1	PAA	2.0	100	27.5 ± 0.6
8	**2a**	1 : 1	PAA	1.0	100	26.7 ± 0.5
9	**2a**	1 : 1	PAA	0.5	100	35.5 ± 0.1
10	**2a**	1 : 1	PAA	0.1	100	42.6 ± 0.3
11	**2a**	1 : 1	PAA	2.0	1000	26.4 ± 0.6
12	**2a**	1 : 1	PDADMAC	2.0	400–500	25.6 ± 0.2
13	**2a**	1 : 1	PDADMAC + PAA (pH 3.9)	0.2 + 0.2	100	67.7 ± 3.7
14	**2a**	1 : 1	—	—	—	13.0 ± 0.8[a]
15	**2a**	1 : 1	PDADMAC + PSS (pH 5.4)	0.2 + 0.2	100	25.8 ± 1.0
16	**2a**	1 : 1	PEI + PAA-Na (pH 7.9)	0.2 + 0.2	100	No reaction
17	**2a**	1 : 1	PEI + PSS (pH 8.3)	0.2 + 0.2	100	No reaction
18	**2a**	1 : 1	PEI + PSS (pH 4.1)[a]	0.2 + 0.2	100	7.7 ± 0.9[a]
19	**2b**	1 : 1	—	—	—	47.2 ± 6.1
20	**2b**	1 : 1	PDADMAC + PAA	0.2 + 0.2	100	40.9 ± 3.6
21	**2c**	1 : 1	—	—	—	28.5 ± 3.4
22	**2c**	1 : 1	PDADMAC + PAA	0.2 + 0.2	100	27.4 ± 3.8
23	**2d**	1 : 1	—	—	—	9.7 ± 0.6
24	**2d**	1 : 1	PDADMAC + PAA	0.2 + 0.2	100	11.7 ± 0.6
25	**2e**	1 : 1	—	—	—	1.8 ± 0.1
26	**2e**	1 : 1	PDADMAC	0.2	100	2.1 ± 0.01
27	**2e**	1 : 1	PAA	0.2	100	2.9 ± 0.01
28	**2e**	1 : 1	PDADMAC + PAA	0.2 + 0.2	100	4.5 ± 0.01
29	**2f**	1 : 1	—	—	—	28.9 ± 1.6
30	**2f**	1 : 1	PDADMAC + PAA	0.2 + 0.2	100	90.6 ± 1.7
31	**2f**	1 : 1	PDADMAC + PSS	0.2 + 0.2	100	40.9 ± 2.3
32	**2f**	1 : 1	PAA	0.2 + 0.2	100	16.3 ± 0.3
33	**2f**	1 : 1	PDADMAC	0.2 + 0.2	100	8.7 ± 0.2

[a] Acetate buffer.

disposes the tip in box T. Another manipulator (gripper, Fig. 2B) is launched by bringing together the finger base and finger parts by the drive, whereas the rotating unit is responsible for an unscrewing event. The gripper performs two tasks: it takes the centrifuge tube from rack D (Fig. 2D) (intended for the storage of closed tubes), transfers it to the positioning device H, unscrews the cap, disposes the cap to the box C, and transfers the tube to rack E or F. In addition, the gripper (Fig. 2B) could transfer the container from rack F to the UV/visible spectrophotometer, assisted by computer vision technology using the OpenCV library for more precise positioning of the gripper unit relative to the cuvette holder of the spectrophotometer (Fig. 2F; full description is given in the SI). This technology was implemented by the video camera located over the gripper, connected to the microcontroller, which sends a QR code of the spectrophotometer, which is set as the reference point (Fig. 2F). To validate the reliability of the developed integrated robotic system, its computer vision accuracy was evaluated under different illumination conditions of ArUco markers, which provide spatial reference of objects. The surface illuminance was measured using a BSIDE L1 digital lux meter (Shenzhen Aimometer, China) with an accuracy of 4%. The ArUco marker illuminance range varying from 0.0 lx (modeling the surface illuminated by a moonless clear night sky with airglow) to 703 lx (illumination during an overcast day) was recorded. ArUco markers were always recognized within the tolerance range of 1–2 cm along the local coordinate system (Fig. S84), which is sufficient for proper working of computer vision in the robotic system.

The system architecture, which is intended to solve inverse kinematic problems related to the correct positioning of the manipulator from rotation parameters of the stepping motor, is as follows (Fig. 2C): computer software generates a task list, which is transferred to the firmware microcontroller equipped with an Arduino IDE program. This program transforms the task list in a *json file to the control signals submitted to each stepping motor, which initiate the operation of corresponding drives. The developed robotic platform provides a graphical interface that represents the platform components and is intuitive for both untrained students and academic staff (Fig. 2E). The user input data from the graphical interface are converted to a *json task list for the Arduino microcontroller (Fig. 2G).

With the robotized platform, we screened the reaction of vanillin **2a** with barbituric acid at reagent concentrations of 1×10^{-3} M tracing the absorbance peak intensity at 405 nm (Table 1). The full scheme of sample preparation is given in Fig. S85. Vanillin **2a** was a starting point for screening due to its representative electron-donating ability among aldehydes **2a–f**, as well as elimination of side reactions, which complicate the

interpretation of reaction outcomes (acid-mediated ring-opening polymerization of furfural **2e**[33] and acid-mediated oligomerization or salt formation of pyrrole (a core of compound **2f**)).[34] Dependence of the concentration of Knoevenagel adduct **3a** on the time of reaction follows the exponential law (Fig. 1C). The reaction rate constant was found to be *ca.* 0.5 L mol^{-1} s^{-1}, which is similar to the rate constants of other condensation reactions in water. As expected, an increase in the vanillin-to-barbituric acid and barbituric acid-to-vanillin ratio enhances the reaction rate. Notably, a three-fold excess of vanillin (entry 5) significantly increases the reaction rate constant up to 1.46 L mol^{-1} s^{-1}, which is presumably caused by the termolecular association of reagents as demonstrated previously.[35] Next, the effect of polyelectrolyte (PE) additives represented by PDADMAC and PAA was evaluated (entries 6–12). One can expect a slight decrease in the rate of Knoevenagel condensation with a decrease in the diffusion coefficient of reagents in PE nanoconfinements.[36–38] Indeed, an increase in the molecular mass distribution of cationic PDADMAC from 100 kDa to 400–500 kDa and anionic PAA from 100 kDa to 1000 kDa (C_{PE} = 2 mg mL^{-1}) decreased the reaction rate constant from 0.50 to 0.31 and 0.26 L mol^{-1} s^{-1}. However, a decrease in the mass concentration of anionic PAA from 2.0 to 0.1 mg mL^{-1} partially recovered the reaction rate constant up to 0.43 L mol^{-1} s^{-1}.

Addition of coacervate complexes of polyelectrolytes (entries 13 and 15–17) showed that the combination of PDADMAC and PAA affords the largest enhancement of the reaction rate constant, taking a value of 0.68 L mol^{-1} s^{-1}. This was attributed to the acidity of the PDADMAC–PAA system (pH 3.8), which is comparable to the one in polyelectrolyte-free reaction mixture (entry 1, pH 3.9) and higher than that of aqueous solutions of other interpolyelectrolyte complexes. This suggestion was verified on the PEI–PSS system, the original acidity (pH 8.3) of which changed through addition of acetate buffer (pH 4.1, entry 18), and the progress of reaction between compounds **1** and **2a** could be observed. Similarly, other aromatic aldehydes reacted with compound **1** at a higher rate in the presence of PDADMAC–PAA interpolyelectrolyte complexes (pH 3.8), which was particularly large in the case of furfural **2f**.

Taken that the described screening and optimization study of the Knoevenagel reaction according to the rate constant is largely based on chemists' intuition and follows a relatively simple one-factor-at-a-time approach,[39] one should be aware of possible overlooked cooperative effects in the parameter space and verify translation of the trends from model reaction between vanillin **2a** and compound **1** into reactions of other aldehydes under study. Therefore, additional experiments were carried out using a robotic platform to distribute the conditions of the Knoevenagel reaction more evenly across aldehyde substrates (Table S17 and Fig. S93–S95). In particular, the aldehyde-to-barbituric acid ratio was screened for veratryl aldehyde **2c** and variation of PAA concentration was screened for ethylvanillin **2b**. As expected, these experiments showed the same trends in the rate of reaction (rate enhancement with an increase in the reagent ratio and suppression with an increase in the polyelectrolyte concentration) as in Table 1. In contrast, expansion of the parameter space of the Knoevenagel reaction by variation of temperature, which was maintained in the cuvette compartment of the UV/visible spectrophotometer, resulted in the mixed dependence of reaction rate constant on temperature. On the one hand, the decreased rate constant of reaction between compounds **1** and **2a** at 5 °C (0.36 L mol^{-1} s^{-1}) could be interpreted as a decrease in the number of effective collisions between reagents. On the other hand, the reaction rate also decreased at 40 °C (0.33 L mol^{-1} s^{-1}) presumably due to the decrease of pH value with an increase in temperature, which illustrates the potential failure of a one-factor-at-a-time approach due to negative cooperative effect of pH and temperature. In spite of this limitation, the reliability of the robotic system in dispensing reagents and transferring the reaction vessel into the cuvette holder of the spectrophotometer was again validated at different temperatures.

The results of optimization of coacervate catalysis of the Knoevenagel reaction at 25 °C (entry 30, Table 1) were used to run the reaction of barbituric acid and furfural **2f** in water at a larger 20 mmol scale at concentrations of PDADMAC and PAA of 0.2 mg mL^{-1}, which afforded the target product **3f** in high yield, which is essentially pure by ^{1}H and ^{13}C NMR spectroscopy, as well as other Knoevenagel adducts run under coacervate catalysis conditions (Fig. S96–S103).

To demonstrate the durability and robustness of the catalytic system under repeated usage, which models its long-term reproducibility in automated workflows on commercial platforms, the following experiment was carried out (Video S1). Equal volumes of 20 mM aqueous solutions of barbituric acid **1** and furfural **2f** in an interpolyelectrolyte complex of 0.4 mg mL^{-1} PDADMAC and 0.4 mg mL^{-1} PAA, which demonstrated the largest enhancement of reaction kinetics in the presence of coacervates, were mixed in a 50-mL centrifuge tube up to a total volume of 20 mL, and the color change of the solution from colorless to yellow and precipitation of the product **3f** were recorded over a 30-min period. After that, the mother liquor was filtered into another centrifuge tube, and new portions of furfural **2f** and 200 mM polyelectrolyte-free aqueous solution of compound **1** (large concentrations were chosen to maintain the volume of the reaction mixture) were added to the mother liquor. By repeating this procedure, a total of ten runs of the Knoevenagel reaction between compounds **1** and **2f** were carried out with a constant quantity of interpolyelectrolyte complex, and the time of completion of precipitate formation always corresponded to *ca.* 30 min, while the color change and precipitate formation were observed immediately after mixing. Notably, the reference experiment in the absence of polyelectrolytes indicated that a color change started after 45 min, while precipitation was observed only within 60–150 min after mixing. This experiment indicates that the catalytic efficiency of the PDADMAC–PAA interpolyelectrolyte complex is preserved over at least 10 cycles of the Knoevenagel reaction.

Analysis of entries 1, 13, and 18 for the reaction between compounds **1** and **2a** indicates that pH is not solely responsible for the reaction rate enhancement. To rationalize experimental

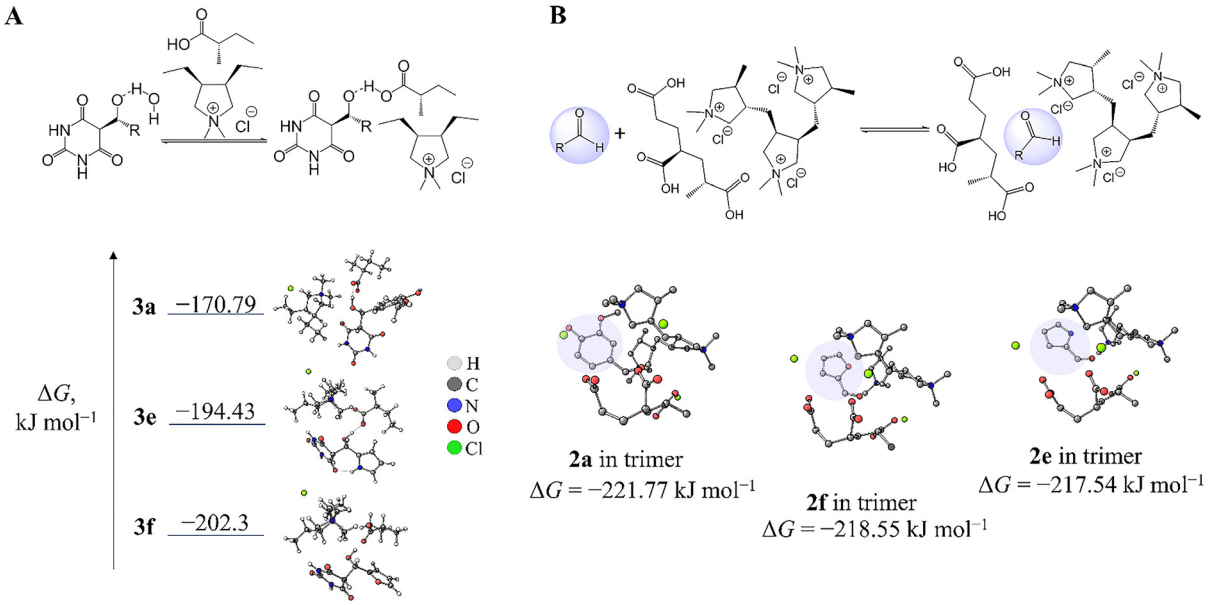

Fig. 3 (A) DFT calculated Gibbs free energies (ΔG) of tetrahedral intermediate formation from aryl aldehydes and barbituric acid in the presence of one repeat unit each of PDADMAC and PAA. (B) DFT calculated Gibbs free energies of aryl aldehyde incorporation into the oligomer model of PDADMAC–PAA interpolyelectrolyte complex.

findings, two hypotheses can be proposed. Firstly, we employed quantum chemical modeling. As a first step, we evaluated the energetic benefit of replacing the aqueous environment of the tetrahedral intermediate formed by the polyelectrolyte environment. The polyelectrolyte model consisted of one unit of PAA in acid form (PAA–Na salt is protonated under Knoevenagel reaction conditions at pH 3.9) and one unit of PDADMAC. This substitution proved to be energetically favorable, as it resulted in a decrease in Gibbs free energy (Fig. 3A). Thus, replacing water molecules with polyelectrolytes leads to stabilization of the system. To improve the accuracy of our model, we constructed a more complex trimer of the interpolyelectrolyte complex comprising three repeat units of PAA and three repeat units of PDADMAC. Given the high conformational flexibility of the system, a comprehensive conformational search was performed using CREST[40] software to identify the most energetically favorable geometry. Following the geometry optimization, the interaction energy between the optimized coacervate trimer and the aldehyde substrate was calculated. The results demonstrate the energetic favorability of substrate inclusion within the polyelectrolyte coacervate, as indicated by the decrease in Gibbs free energy upon complex formation (Fig. 3B).

Secondly, DLS measurements were carried out to confirm the formation of the coacervate droplets in the presence of oppositely charged PDADMAC and PAA polyelectrolytes. First a series of measurements was conducted in 0.2 mg mL^{-1} PDADMAC–PAA system in water, in which particle size distribution by intensity was analyzed immediately after mixing PDADMAC and PAA solutions in water (0 min) and after 30 min of mixing. According to the S-shaped correlogram, well-defined particles are formed (Fig. S104A). A bimodal particle size distribution (with hydrodynamic diameter values at *ca.* 85 nm and 390 nm) with particle sizes gradually increasing over a 30-min period indicates the formation of the coacervate phase of interpolyelectrolyte complex with a size of *ca.* 100–400 nm, which can represent a confined space for the enhanced kinetics of the Knoevenagel reaction. In the second series of measurements, barbituric acid and vanillin **2a** were added to the PDADMAC–PAA system, and particle size distribution was again analyzed after mixing (0 min) and after 10 min and 30 min, as well as after 300 min of mixing (Fig. S104B). Again, the nanoparticles attributed to the PDADMAC–PAA interpolyelectrolyte complex were detected in a mean size range of 50–70 nm, but the size distribution curve showed increased complexity over time as compared to the first series of measurements in the range of 100 nm–10 μm, which is due to the presence of suspended vanillin barbiturate particles. Thus, the Knoevenagel reaction components did not suppress the formation of the PDADMAC–PAA interpolyelectrolyte complex even after a prolonged period of exposure (which simulates long-term stability testing of the complex), which supports the involvement of coacervates in the Knoevenagel reaction.

In summary, we demonstrate the use of two articulated robotic manipulators, a pipette-based dispenser and an electromechanical gripper, designed to automate key operations in liquid-phase organic synthesis. The dispensing module is highly versatile and can be applied to a wide range of reactions involving liquid reagents, which dominate both analytical and preparative laboratory workflows. The gripper module serves as a universal actuator capable of performing diverse mechanical operations, including transferring glassware, handling solid reagents, opening containers, and interfacing with analytical instruments. This modularity provides a strong foundation for adapting the platform to other classes of chemical

transformations, including multi-step synthesis, solid–liquid extractions, and heterogeneous catalysis workflows. However, a number of limitations must be addressed to scale the system further. These include the lack of integrated temperature or pressure control for thermochemically sensitive reactions, limited precision in microfluidic or nanoliter-scale operations, and the absence of feedback-based autonomous decision-making for real-time protocol adjustment. To overcome these limitations, future research may focus on incorporating modular temperature/pressure control units, integrating machine-learning algorithms for real-time adaptive optimization, and expanding the manipulator range to include syringe pumps, pH electrodes, and solid-phase handling tools. Ultimately, the platform serves as a proof-of-concept for customizable, low-cost automation of organic workflows. Its open-source nature enables further community-driven development, making it suitable for educational, exploratory, and even semi-industrial applications where flexibility is prioritized over throughput.

Experimental

Materials

Barbituric acid **1** and aldehydes **2b–e** (all of reagent grade, Sigma-Aldrich) and **2a** (reagent grade, SRL) were used as supplied, while furfural **2f** (reagent grade, Komponent-Reaktiv) was distilled under atmospheric pressure from 7% (w/w) Na_2CO_3 and then fractionally distilled under vacuum. Deionized water (18 MΩ cm) or acetate buffer (pH 4.1), which was prepared from 0.5 M solutions of CH_3COOH (reagent grade, Lenreaktiv) and CH_3COONa (reagent grade, Lenreaktiv) mixed at a 4.5-to-1 ratio (v/v), were used as solvents. The PEs – branched polyethyleneimine (PEI, $M_w \approx$ 750k, 50% (w/v) solution), poly(sodium 4-styrenesulfonate) (PSS, $M_w \approx$ 70k, powder), poly(acrylic acid) (PAA, $M_w \approx$ 100k, 35% (w/v) solution; $M_w \approx$ 1000k, powder), poly(diallyldimethylammonium chloride) (PDADMAC, $M_w \approx$ 400–500k, 20% (w/v) solution; $M_w <$ 100k, 35% (w/v) solution), and poly(acrylic acid) sodium salt (PAA-Na, $M_w \approx$ 100k, 50% (w/v) solution) – were purchased from Sigma-Aldrich and used as received.

Camera calibration and ArUco detection toolkit

The developed camera calibration and ArUco detection toolkit employs Python libraries, such as NumPy v1.24.0,[41] OpenCV-contrib-python v4.8.0, PyYAML v5.4.1, and Loguru v0.7.0. ArUco markers were generated using a cv2.aruco module using a DICT_4 × 4_50 dictionary. To capture video stream and determine attitude of markers, a USB 2.0 Canyon CNS-CWC5 web camera (Asbisc Enterprises, Limassol, Cyprus), with a resolution of 1920 × 1080 px at 30 fps, was used. Briefly, the camera was calibrated before measurements to eliminate barrel and pincushion distortions of objective and compensate for principal point bias and scale difference. Calibration was performed using a 9 × 6 OpenCV chessboard (cell size = 25 mm) printed on matte paper. The internal calibration parameters and radial and tangential distortion coefficients were calculated using a cv2.calibrateCamera function of the OpenCV library according to a series of images acquired at different camera angles and distances and saved to calib_params.npz file for subsequent use. The detection of ArUco markers in video stream was implemented using the cv2.aruco.detectMarkers function, while evaluation of their coordinates and orientation was implemented using the cv2.aruco.estimatePoseSingleMarkers function. Visualization of the orientation of ArUco markers was carried out using the cv2.drawFrameAxes function, which represents the local coordinate system.

Spectrophotometric monitoring of reaction kinetics

Reaction mixtures for kinetic experiments without PEs were prepared by mixing equal volumes of solutions of **2a–f** and **1** to the final reagent concentrations of 1 mM (as a part of optimization, molar reagent ratios of 1 : 1, 1 : 2, and 1 : 3 were used). When there were PE additives, the mixing procedure followed the one illustrated in Fig. S85. Briefly, 10 mM of compound **1** and 10 mM of compound **2** were mixed separately with equal volumes of PE solutions (4 mg mL^{-1}) to afford solutions 1 and 2, respectively. These solutions were combined to afford the reaction mixture with the following final concentrations: reagents, 2.5 mM; and PEs, 1 mg mL^{-1}. The interpolyelectrolyte complex (IPEC) was prepared by mixing equal volumes of 0.8 mg mL^{-1} of cationic and anionic PEs in order to avoid precipitation (Fig. S85). A total of 4 mM of compound **1** and 4 mM of compound **2** were mixed separately with equal volumes of IPEC (0.4 mg mL^{-1}). After taking subsequent steps, the reaction mixture had the following final concentrations: reagents, 1 mM; and Pes, 0.1 mg mL^{-1} (Fig. S85). The pH value was controlled using a pH meter (HI 2210, HANNA Instruments) pre-calibrated for standard buffer solutions with pH 4.01 (potassium hydrogen phthalate), 7.01 (disodium phosphate + monopotassium phosphate) and 10.01 (sodium bicarbonate + sodium carbonate). UV/visible absorption spectra of the reaction mixtures were recorded in 1-cm plastic cuvettes using a Shimadzu spectrophotometer in the wavelength range of 350–600 nm within a 1-min interval, with monitoring of the band intensity at *ca.* 405 nm (reactions with **2a–e**) and 390 nm (reaction with **2f**). The UV/visible absorption spectra were recorded using UV Probe software and processed in Origin. The following spectral processing steps were undertaken to derive the rate constant (Fig. 1C). The time-resolved baseline-corrected UV/visible absorption spectra (1) were transformed into a concentration *vs.* time graph for the Knoevenagel adduct (2) using the corresponding molar absorption coefficient (eqn (1)):

$$\varepsilon = \frac{A}{Cl} \tag{1}$$

where A is the absorbance, l is the optical path length, and C is the concentration of the product of reaction.

The graph (2) was reconstructed into a plot of inverse current concentration of compound **1** from time (3) using eqn (2):

$$\frac{1}{C_1} = \frac{1}{C_0 - C} \tag{2}$$

where C_1 is the reagent concentration, C_0 is initial reagent concentration, and C is the concentration of the product of reaction.

The slope of the curve (3), which is the reaction rate constant, was determined by linear fitting of the 0–5 min interval.

Millimolar scaling of Knoevenagel adduct

In the case of scaling up the reaction, concentrations of barbituric acid and aldehydes of 20 mM were used, and concentrations of polyelectrolytes were 0.2 mg mL^{-1}. The completeness of the reaction was evaluated by the TLC method. The eluent was heptane and ethyl acetate (1 : 1).

Computational details

The conformational search was performed using the CREST[40] software (version 2.12), employing the GFN2-xTB method[42] with the ALPB[43] solvation model with water as the solvent. To ensure comprehensive sampling of the conformational space of noncovalent complexes, the NCI (noncovalent interactions) flag was enabled. All DFT calculations were carried out with the ORCA 5.0.4 program package.[44] Geometry optimizations and frequency calculations (with no imaginary frequencies detected in all cases) were carried out at the B3LYP-D3/def2-SVP level of theory. The calculations employed tight optimization and self-consistent field convergence criteria to ensure accurate results. Solvent effects were modeled using the conductor-like polarizable continuum model (CPCM) with water as the solvent. The default convergence tolerances for the geometry optimization procedure were used: energy change = 1.0×10^{-6} E_h, maximal gradient = 1.0×10^{-4} E_h $Bohr^{-1}$, RMS gradient = 3.0×10^{-5} E_h $Bohr^{-1}$, maximal displacement = 1.0×10^{-3} Bohr, and RMS displacement = 6.0×10^{-4} Bohr. To further refine the obtained geometries and evaluate interaction energies, the aldehyde reagent was incorporated into the optimized polyelectrolyte coacervate, and the inclusion complex was reoptimized using the r^2SCAN-3c composite method.[45] The Gibbs free energies were calculated to confirm the stability of the resulting assemblies.

Dynamic light scattering

DLS of 1-mL solutions of 0.2 mg mL^{-1} PDADMAC–PAA system with and without 1 mM vanillin–barbituric acid system was conducted at 26 °C in a round cell using a Photocor Compact-Z particle size analyzer (Moscow, Russia) at a scattering angle of 90° and laser wavelength of 637 nm. The measured autocorrelation functions were analyzed with built-in Photocor software applying third-order cumulant expansion methods. The effective hydrodynamic radius (R_H) was calculated according to the Einstein–Stokes equation $D = k_B T/6\pi\eta R_H$, in which D is the diffusion coefficient, k_B is the Boltzmann constant, T is the absolute temperature, and η is the viscosity.

Conclusions

The work is focused on transformative materials research. In this study, we developed a low-cost, 3D-printed robotic platform integrated with computer vision tools to automate the optimization of Knoevenagel reactions. The platform combines gripper and dispenser manipulators with open-source Python-based software, enabling precise reagent mixing, kinetic spectrophotometric monitoring, and high-throughput screening of reaction conditions. A step-by-step guide is provided in the SI. The system successfully automated the entire workflow, from reagent handling to data acquisition, demonstrating improved reproducibility and efficiency compared to manual methods. The use of computer vision ensured accurate positioning of the gripper for spectrophotometric analysis.

The following differences between the open-source robotic system in this work and commercially available high-cost proprietary platforms can be highlighted. While commercially available robotic systems are known for their high precision, durability, and industrial-grade reliability, they often lack flexibility required for academic and industrial exploratory research. In particular, proprietary platforms typically limit user access to hardware and software customization, hampering their integration with unconventional workflows or emerging technologies (such as coacervate-mediated catalysis). In contrast, the proposed open-source 3D-printed robotic platform allows for rapid prototyping and easy mechanical reconfiguration of the system for a particular task due to its modular design. Furthermore, the integration of Python-based open software and Arduino microcontroller firmware provides a straightforward incorporation of third-party tools (computer vision algorithms, spectroscopic interfaces, or new actuators), a level of customization not typical of closed-source systems. Most importantly, our system demonstrates for the first time the integration of robotic automation with coacervate catalysis, a largely unexplored domain in robotic chemistry and a particularly attractive direction of soft-matter-mediated organic reactions. This work would reinforce the employment of low-cost, open-access robotic platforms in exploration of chemical reaction space and advance the adoption of novel reaction environments in automated workflows.

The novelty of this work lies in both technical and conceptual integration. Technically, we developed a robotic system that combines articulated manipulators with computer vision and an intuitive user interface, allowing fully automated reaction handling, including solid and liquid transfers, vessel manipulation, and spectroscopic monitoring. Conceptually, this is the first report of robotized screening of polyelectrolyte coacervates as catalytic media for the Knoevenagel reaction. This opens a path for the high-throughput study of soft-matter environments in organic synthesis, a topic that remains underexplored in the current literature. Additionally, the modularity of our system allows its adaptation for educational purposes, where cost, reproducibility, and transparency are critical. We believe this synergy of accessible hardware and novel reaction media represents a meaningful step toward democratizing robotic chemistry.

Screening of reagent ratios and use of polyelectrolyte coacervate catalysis revealed that a three-fold excess of vanillin significantly accelerated the reaction (rate constant: 1.46 L mol^{-1} s^{-1}). Polyelectrolyte crowding effects were systematically

investigated with PDADMAC–PAA coacervates at pH 3.9 enhancing the reaction rate (0.677 L mol^{-1} s^{-1}), while other combinations (*e.g.*, PEI–PSS at pH 8.3) inhibited reactivity. Electron-donating groups (*e.g.*, furfural) exhibited faster rates, whereas pyrrole derivatives showed slower kinetics, corroborated by DFT calculations of Gibbs free energies for intermediate formation and substrate incorporation into coacervate models.

Author contributions

ASN (Anna S. Nebalueva), APG, AAM, DVA, and EVS suggested the experimental system for dataset collection and provided the initial methodology and experiments for robot programming. ASN (Alexander S. Novikov) and DVE performed DFT calculations and theoretical analysis for coacervate catalysis. AAN, BSV, AMZ, and ISP conducted 3D modeling, robot production, and programming. AAS and AVM proposed the methodology for dataset collection using the robotic system and were responsible for the robotization of chemical technology and machine vision for the robotic arm. All authors wrote their respective sections and approved the final manuscript.

Conflicts of interest

There are no conflicts of interest to declare.

Data availability

NMR spectra of Knoevenagel adducts **3a–f**, UV/visible spectra of the reaction mixtures, instructions for manipulators' assembly, description of manipulator firmware and computer vision-assisted pose tracking and ArUco detection toolkit, as well as Cartesian atomic coordinates for all optimized model structures, are included in the SI. Supplementary information: Codes, instruction for 3D robotic arm production, dataset collection procedure. See DOI: **https://doi.org/10.1039/d5mh00559k**.

The program codes for the manipulators and computer vision are available in the GitHub repository at **https://github.com/Zenkin/robotic-Knoevenagel-optimization**.

Acknowledgements

The authors acknowledge grant no. FSER-2025-0026 for financial support. For infrastructural support, DVA thanks the Ministry of Education (Singapore) through the Research Centre of Excellence program (Award EDUN C-33-18-279-V12, Institute for Functional Intelligent Materials).

References

1 A. I. Oparin and A. Synge, *The Origin of Life on Earth*, Academic, New York, United States, 1957.
2 P. Zhao, F. Qu, H. Fu, J. Zhao, J. Xu, Y.-P. Ho, M. K. Chan and L. Bian, *J. Am. Chem. Soc.*, 2023, **145**, 3312–3317.
3 B. Valley, B. Jing, M. Ferreira and Y. Zhu, *ACS Appl. Mater. Interfaces*, 2019, **11**, 7472–7478.
4 I. B. A. Smokers, B. S. Visser, A. D. Slootbeek, W. T. S. Huck and E. Sprujit, *Acc. Chem. Res.*, 2024, **57**, 1885–1895.
5 A. N. Kwant, J. S. Es Sayed, M. Kamperman, J. K. Burgess, D.-J. Slebos and S. D. Pouwels, *Adv. Healthcare Mater.*, 2025, **14**, 2402340.
6 A. A. Baldina, L. V. Pershina, U. V. Noskova, A. A. Nikitina, A. A. Muravev, E. V. Skorb and K. G. Nikolaev, *Polymers*, 2022, **14**, 5145.
7 C. M. Green, D. Sementa, D. Mathur, J. S. Melinger, P. Deshpande, S. Elbaum-Garfinkle, I. L. Medintz, R. V. Ulijn and S. A. Díaz, *Commun. Chem.*, 2024, **7**, 49.
8 A. A. Evdokimov, A. A. Baldina, A. A. Nikitina, T. A. Aliev, A. M. Zenkin, M. V. Zhukov, I. S. Pantyukhin, E. V. Skorb and A. A. Muravev, *Sens. Bio-Sens. Res.*, 2025, **47**, 100744.
9 H. Zhang, C. Wang, G. Zhu and N. S. Zacharia, *ACS Appl. Mater. Interfaces*, 2016, **8**, 26258–26265.
10 E. V. Kukhtenko, F. V. Lavrentev, V. V. Shilovskikh, P. I. Zyrianova, S. I. Koltsov, A. S. Ivanov, A. S. Novikov, A. A. Muravev, K. G. Nikolaev, D. V. Andreeva and E. V. Skorb, *Polymers*, 2023, **15**, 45.
11 W. Yim, Z. Jin, Y.-C. Chang, C. Brambila, M. N. Creyer, C. Ling, T. He, Y. Li, M. Retout, W. F. Penny, J. Zhou and J. V. Jokerst, *Nat. Commun.*, 2024, **15**, 7295.
12 V. A. Kabanov, *Russ. Chem. Rev.*, 2005, **74**, 3–20.
13 B. Drobot, J. M. Iglesias-Artola, K. Le Vay, V. Mayr, M. Kar, M. Kreysing, H. Mutschler and T.-Y. Dora Tang, *Nat. Commun.*, 2018, **9**, 3643.
14 M. I. Jacobs, E. R. Jira and C. M. Schroeder, *Langmuir*, 2021, **37**, 14323–14335.
15 V. M. Kolb, M. Swanson and F. M. Menger, *Proc. SPIE*, 2012, **8521**, 85210E.
16 S. Cao, T. Ivanov, J. Heuer, C. T. J. Ferguson, K. Landfester and L. C. da Silva, *Nat. Commun.*, 2024, **15**, 39.
17 B. Saini, S. Singh and T. K. Mukherjee, *ACS Appl. Mater. Interfaces*, 2021, **13**, 51117–51131.
18 R. L. Greenaway, V. Santolini, M. J. Bennison, B. M. Alston, C. J. Pugh, M. A. Little, M. Miklitz, E. G. B. Eden-Rump, R. Clowes, A. Shakil, H. J. Cuthbertson, H. Armstrong, M. E. Briggs, K. E. Jelfs and A. I. Cooper, *Nat. Commun.*, 2018, **9**, 2849.
19 B. Burger, P. M. Maffettone, V. V. Gusev, C. M. Aitchison, Y. Bai, X. Wang, X. Li, B. M. Alston, B. Li, R. Clowes, N. Rankin, B. Harris, R. S. Sprick and A. I. Cooper, *Nature*, 2020, **583**, 237–241.
20 S. Asche, G. J. T. Cooper, G. Keenan, C. Mathis and L. Cronin, *Nat. Commun.*, 2021, **12**, 3547.
21 N. L. Bell, F. Boser, A. Bubliauskas, D. R. Willcox, V. S. Luna and L. Cronin, *Nat. Chem. Eng.*, 2024, **1**, 180–189.
22 S. Rohrbach, M. Šiaučiulis, G. Chisholm, P.-A. Pirvan, M. Saleeb, S. H. M. Mehr, E. Trushina, A. I. Leonov, G. Keenan, A. Khan, A. Hammer and L. Cronin, *Science*, 2022, **377**, 172–180.
23 S. Steiner, J. Wolf, S. Glatzel, A. Andreou, J. M. Granda, G. Keenan, T. Hinkley, G. Aragon-Camarasa, P. J. Kitson, D. Angelone and L. Cronin, *Science*, 2018, **363**, 144.
24 V. P. Ananikov, *Artif. Intell. Chem.*, 2024, **2**, 100075.

25 C. J. Brown, T. McGlone, S. Yerdelen, V. Srirambhatla, F. Mabbott, R. Gurung, M. L. Briuglia, B. Ahmed, H. Polyzois, J. McGinty, F. Perciballi, D. Fysikopoulos, P. MacFhionnghaile, H. Siddique, V. Raval, T. S. Harrington, A. D. Vasilleiou, M. Robertson, E. Prasad, A. Johnston, B. Johnston, A. Nordon, J. S. Srai, G. Halbert, J. H. ter Horst, C. J. Price, C. D. Rielly, J. Sefcik and A. J. Florence, *Mol. Syst. Des. Eng.*, 2018, **3**, 518–549.
26 A. M. Lunt, H. Fakhruldeen, G. Pizzuto, L. Longley, A. White, N. Rankin, R. Clowes, B. Alston, L. Gigli, G. M. Day, A. I. Copper and S. Y. Chong, *Chem. Sci.*, 2024, **15**, 2456–2463.
27 R. P. Badiger, V. N. Patil, S. Marathe, N. Ananya, P. R. Shreshta Srinivas, M. J. Venkatarangan, D. Sethuram, S. Prasad and S. N. Suma, in *10th International Conference on Control, Automation and Robotics (ICCAR)*, IEEE, Singapore, Singapore, 2024, pp. 159–165.
28 S. Lo, S. G. Baird, J. Schrier, B. Blaiszik, N. Carson, I. Foster, A. Aguilar-Granda, S. V. Kalinin, B. Maruyama, M. Politi, H. Tran, T. D. Sparks and A. Aspuru-Guzik, *Dig. Disc.*, 2024, **3**, 842–868.
29 A. I. Hanopolskyi, T. A. Mikhnevich, A. Paikar, B. Nutkovich, I. Pinkas, T. Dadosh, B. S. Smith, N. Orekhov, E. V. Skorb and S. N. Semenov, *Chem*, 2023, **9**, 3666–3684.
30 B. B. Sokmen, S. Ugras, H. Y. Sarikaya, H. I. Ugras and R. Yanardag, *Appl. Biochem. Biotechnol.*, 2013, **171**, 2030–2039.
31 A. S. Nebalueva, A. A. Timralieva, R. V. Sadovnichii, A. S. Novikov, M. V. Zhukov, A. S. Aglikov, A. A. Muravev, T. V. Sviridova, V. P. Boyarskiy, A. L. Kholkin and E. V. Skorb, *Molecules*, 2022, **27**, 5659.
32 J. Yu, D. Shen, H. Zhang and Z. Yin, *Bioconjugate Chem.*, 2018, **29**, 1016–1020.
33 A. O. C. Iroegbu and S. S. Ray, *J. Polym. Sci.*, 2024, **62**, 1044–1060.
34 H. Hartmann and J. Schönewerk, *Chem. Select*, 2023, **8**, e202301087.
35 S. Lukin, M. Tireli, I. Lončarić, D. Barišić, P. Šket, D. Vrsaljko, M. di Michiel, J. Plavec, K. Užarević and I. Halasz, *Chem. Commun.*, 2018, **54**, 13216–13219.
36 K. Yang, K. G. Nikolaev, X. Li, A. Ivanov, J. H. Bong, I. Erofeev, U. M. Mirsaidov, V. G. Kravets, A. N. Grigorenko, S. Zhang, X. Qiu, K. S. Novoselov and D. V. Andreeva, *Proc. Natl. Acad. Sci. U. S. A.*, 2024, **121**, e2414449121.
37 K. Yang, Z. Hu, X. Li, K. Nikolaev, G. K. Hong, N. Mamchik, I. Erofeev, U. M. Mirsaidov, A. H. Castro Neto, D. J. Blackwood, D. G. Shchukin, M. Trushin, K. S. Novoselov and D. V. Andreeva, *Proc. Natl. Acad. Sci. U. S. A.*, 2023, **120**, e2307618120.
38 K. Yang, Q. Wang, K. S. Novoselov and D. V. Andreeva, *Nanoscale Horiz.*, 2023, **8**, 1243–1252.
39 C. J. Taylor, A. Pomberger, K. C. Felton, R. Grainger, M. Barecka, T. W. Chamberlain, R. A. Bourne, C. N. Johnson and A. A. Lapkin, *Chem. Rev.*, 2023, **123**, 3089–3126.
40 P. Pracht, F. Bohle and S. Grimme, *Phys. Chem. Chem. Phys.*, 2020, **22**, 7169.
41 C. R. Harris, K. J. Millman, S. J. van der Walt, R. Gommers, P. Virtanen, D. Cournapeau, E. Wieser, J. Taylor, S. Berg, N. J. Smith, R. Kern, M. Picus, S. Hoyer, M. H. van Kerkwijk, M. Brett, A. Haldane, J. Fernández del Río, M. Wiebe, P. Peterson, P. Gérard-Marchant, K. Sheppard, T. Reddy, W. Weckesser, H. Abbasi, C. Gohlke and T. E. Oliphant, *Nature*, 2020, **585**, 357–362.
42 C. Bannwarth, S. Ehlert and S. Grimme, *J. Chem. Theory Comput.*, 2019, **15**, 1652.
43 S. Ehlert, M. Stahn, S. Spicher and S. Grimme, *J. Chem. Theory Comput.*, 2021, **17**, 4250.
44 F. Neese, *Wiley Interdiscip. Rev. Comput. Mol. Sci.*, 2012, **2**, 73–78.
45 S. Grimme, A. Hansen, S. Ehlert and J.-M. Mewes, *J. Chem. Phys.*, 2021, **154**, 064103.

